A practical adaptive grid method for the Allen–Cahn equation

Darae Jeong [a], Yibao Li [b], Yongho Choi [c], Chaeyoung Lee [d], Junxiang Yang [d], Junseok Kim [d],*

[a] *Department of Mathematics, Kangwon National University, Gangwon-do 24341, Republic of Korea*
[b] *School of Mathematics and Statistics, Xi'an Jiaotong University, Xi'an 710049, China*
[c] *Department of Mathematics and Big Data, Daegu University, Gyeongsan-si, Gyeongsangbuk-do 38453, Republic of Korea*
[d] *Department of Mathematics, Korea University, Seoul 02841, Republic of Korea*

ARTICLE INFO

ABSTRACT

We present a simple and practical adaptive finite difference method for the Allen–Cahn (AC) equation in the two-dimensional space. We use a temporally adaptive narrow band domain embedded in the uniform discrete rectangular domain. The narrow band domain is defined as a neighboring region of the interface. We employ a recently developed explicit hybrid numerical scheme for the AC equation. Therefore, the computational algorithm on the narrow band discrete domain is simple and fast. We demonstrate the high performance of the proposed adaptive method for the AC equation through various computational experiments.

© 2021 Elsevier B.V. All rights reserved.

1. Introduction

We consider a simple and practical adaptive finite difference method (FDM) for the following Allen–Cahn (AC) equation in two-dimensional space:

$$\frac{\partial \phi(\mathbf{x}, t)}{\partial t} = \frac{\phi(\mathbf{x}, t) - \phi^3(\mathbf{x}, t)}{\epsilon^2} + \Delta \phi(\mathbf{x}, t), \quad \mathbf{x} \in \Omega, \tag{1}$$

$$\mathbf{n} \cdot \nabla \phi(\mathbf{x}, t) = 0, \quad \mathbf{x} \in \partial \Omega, \tag{2}$$

where $\phi(\mathbf{x}, t)$ is the order parameter at space $\mathbf{x}$ and time t in a bounded domain Ω, ϵ is a parameter, $\mathbf{n}$ is normal to $\partial \Omega$. Allen and Cahn introduced the AC equation to represent the motion of anti-phase boundaries in crystalline solids [1]. The AC equation has been applied to many problems and applications such as image inpainting [2], mean curvature flows [3,4], phase transitions [5], multimaterial topology optimization [6], image segmentation [7], and crystal growth [8].

Therefore, to understand and apply the AC dynamics we need the efficient and accurate numerical solutions of the AC equation. Many numerical methods for the AC equations have been developed. For example, some of recent works are as follows. A linearized second-order FDM was developed and discrete boundedness stability was established in [9]. The authors in [10] presented a linearized high-order compact FDM for the three-dimensional AC equation. The authors in [11] proposed a reproducing kernel method using the FDM and the Quasi-Newton method to solve the AC equation. A semi-analytical Fourier spectral method for the AC equation was presented in [12]. The fast FDM and the fast Fourier spectral method were adopted to effectively solve the time fractional AC equation in [13]. In [14], the authors reduced the time fractional AC equation to ordinary differential equation and solve the reduced equation by using an explicit power

---

* Corresponding author.
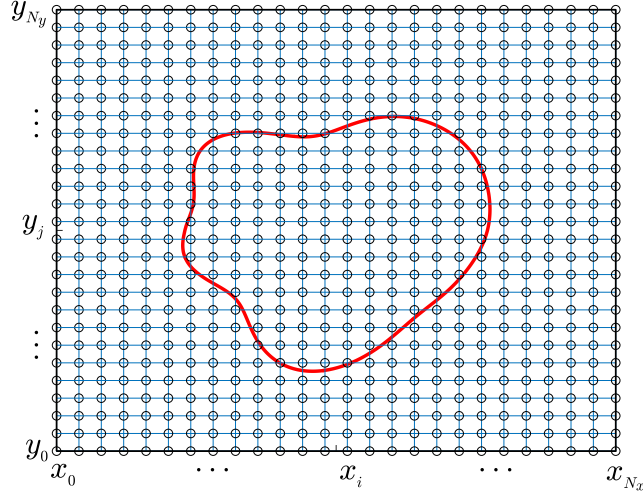 *E-mail address:* cfdkim@korea.ac.kr (J. Kim).

Fig. 1. Schematic of computational domain Ω_h (dot) and the contour line by a given zero-level set of ϕ (red line).

series. Efficient adaptive second-order in time approximations of the AC equation was proposed in [15]. A conforming finite element method (FEM) for the numerical solution of the AC equation was developed in [16]. The authors in [17] developed an operator-splitting unconditionally stable FEM for the two- and three-dimensional AC equation. In [18], the authors designed, analyzed, and showed an unconditionally energy stable second-order FEM for solving the AC equation.

Distinguishing features of the evolutionary dynamics of the AC equation are: (1) small portion for the interfacial transition region compared to the whole domain and (2) size of the transition layer decreases as time evolves. Therefore, it is natural to compute the AC equation on an adaptive grid. In this article, by using a recently developed adaptive mesh method [19] and a hybrid explicit scheme [20], we propose a practical adaptive grid method for the AC equation, which is simple, fast, and accurate.

The contents of this article are as follows. In Section 2, we present the proposed numerical scheme and its solution algorithm for the AC equation. We present numerical results of motion by mean curvature in Section 3. Conclusions are drawn in Section 5.

2. Numerical method

We now describe an adaptive explicit hybrid FDM for Eq. (1) on the computational domain $\Omega = (a, b) \times (c, d)$. First, we define the discrete global domain $\Omega_h = \{(x_i, y_j)| \ x_i = a + hi, \ y_j = c + dj \ \text{for} \ 0 \le i \le N_x, \ 0 \le j \le N_y\}$ according to an uniform space grid size $h = (b - a)/N_x = (d - c)/N_y$, where N_x and N_y are positive integers (see Fig. 1).

Then, we let ϕ_{ij}^n denote the approximation of the solution $\phi(x_i, y_j, n\Delta t)$ of Eq. (1), where Δt is the time step. As have been mentioned, ϕ is the order parameter having the value between -1 and 1 as shown in Fig. 2(a). And we define the interface of two phases as the zero-level set of ϕ. Using these property of ϕ, we define new computational domain.

For given $\gamma > 0$ and integer $m > 0$, we introduce the following time-dependent adaptive narrow band domain $\tilde{\Omega}_h^n$ [19] as

$$\tilde{\Omega}_h^n = \left\{(x_{i+p}, y_{j+q})| \ |\phi_{ij}^n| \le \gamma \ \text{ for } \ \forall i, j \text{ and } -m \le p, q \le m\right\}.$$

Here, the narrow band domain $\tilde{\Omega}_h^n$ is embedded in the discrete computational domain Ω_h. Fig. 2(b) illustrates the narrow band domain $\tilde{\Omega}_h^n$.

Now, we solve the governing Eq. (1) on the narrow band domain $\tilde{\Omega}_h^n$. First, we initialize ϕ^0 on the computational domain Ω_h. Then, we define the narrow band domain $\tilde{\Omega}_h^n$ with the given ϕ^n. By taking the following explicit hybrid procedure [20], we solve ϕ^{n+1} with the given ϕ^n. For all $(x_i, y_j) \in \tilde{\Omega}_h^n$, we compute a temporary value ϕ_{ij}^*:

$$\frac{\phi_{ij}^* - \phi_{ij}^n}{\Delta t} = \Delta_h \phi_{ij}^n = \frac{\phi_{i+1,j}^n + \phi_{i-1,j}^n - 4\phi_{ij}^n + \phi_{i,j+1}^n + \phi_{i,j-1}^n}{h^2}.$$

After we obtain ϕ_{ij}^*, taking it as the initial conditions, i.e., $\psi_{ij}(0) = \phi_{ij}^*$, for the following ordinary differential equations and solve them analytically:

$$\frac{d\psi_{ij}(t)}{dt} = \frac{\psi_{ij}(t) - (\psi_{ij}(t))^3}{\epsilon^2}$$

and then we get $\phi_{ij}^{n+1} = \psi_{ij}(\Delta t) = \phi_{ij}^* / \sqrt{(\phi_{ij}^*)^2 + [1 - (\phi_{ij}^*)^2]e^{-2\Delta t/\epsilon^2}}$.
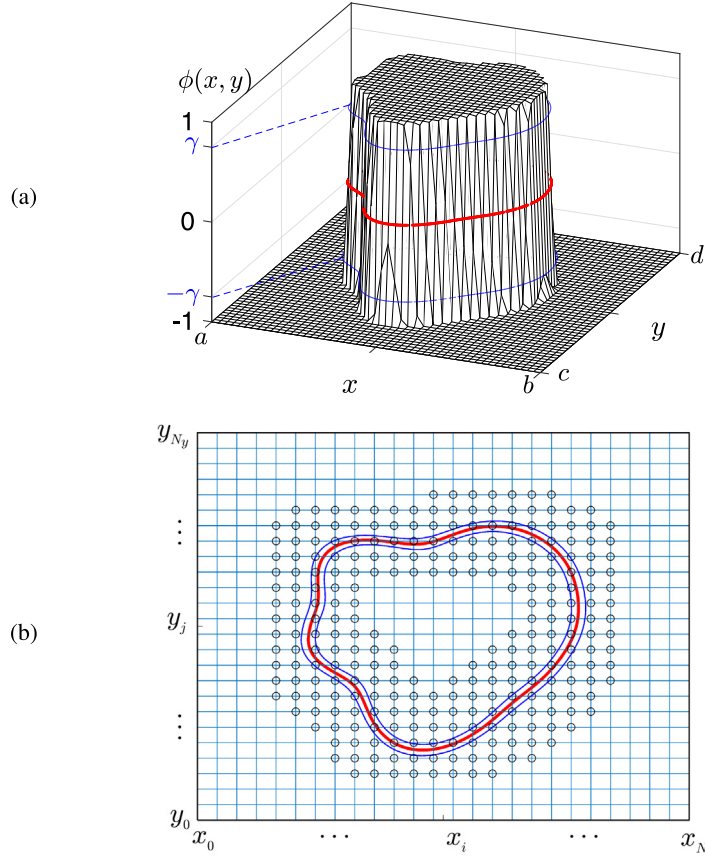
Fig. 2. Schematic of (a) ϕ and (b) narrow band domain $\tilde{\Omega}_h^n$ (dot) and the contour line by a given zero-level set of ϕ (red line).

3. Numerical experiments

In this study, we implement several numerical experiments. Here, we use the notation $\epsilon_l = lh/[2\sqrt{2}\tanh^{-1}(0.9)]$ for the interfacial parameter ϵ that means approximately lh transition layer across the interface.

3.1. Evolution of a circular interface

Because there are only limited closed-form solutions for the AC-type equation [21], as a test problem for the accuracy of the numerical algorithm, we consider the temporal evolution of a circle whose radius is $R(t)$ at time t under moving by mean curvature. As ϵ approaches zero, the AC equation is known that the zero-level contour of ϕ evolves to the normal direction velocity, i.e., $dR(t)/dt = -1/R(t)$ [1]. Therefore, if the initial radius of a circle is R_0, then the radius follows the analytical movement as $R(t) = \sqrt{R_0^2 - 2t}$. With the property of the solution for the AC equation, we verify accuracy of the numerical solution.

We set the initial condition as $\phi(x, y, 0) = \tanh[(R_0 - \sqrt{x^2 + y^2})/(\sqrt{2}\epsilon)]$ on $\Omega = (-50, 50) \times (-50, 50)$. Here, the initial radius is given by $R_0 = 35$ and the other numerical parameters are used as $\epsilon = \epsilon_8$, $N_x = N_y = 400$, $h = 0.25$, $\Delta t = 0.2h^2$. Fig. 3(a) and (b) show the temporal evolutions of zero-level contour of ϕ and radius $R(t)$, respectively. Especially, in Fig. 3(b), we can observe that the numerical solutions are in good agreement with the analytic solutions. Also, Fig. 3(c)–(e) represent the discrete narrow band domains $\tilde{\Omega}_h^n$ used at $t = 0$, 350, and 600, respectively.

3.2. Evolution of a star-shape interface

Next, let us consider the evolution of a star-shaped interface under the motion by mean curvature. The initial condition on $\Omega = (-50, 50) \times (-50, 50)$ is given as

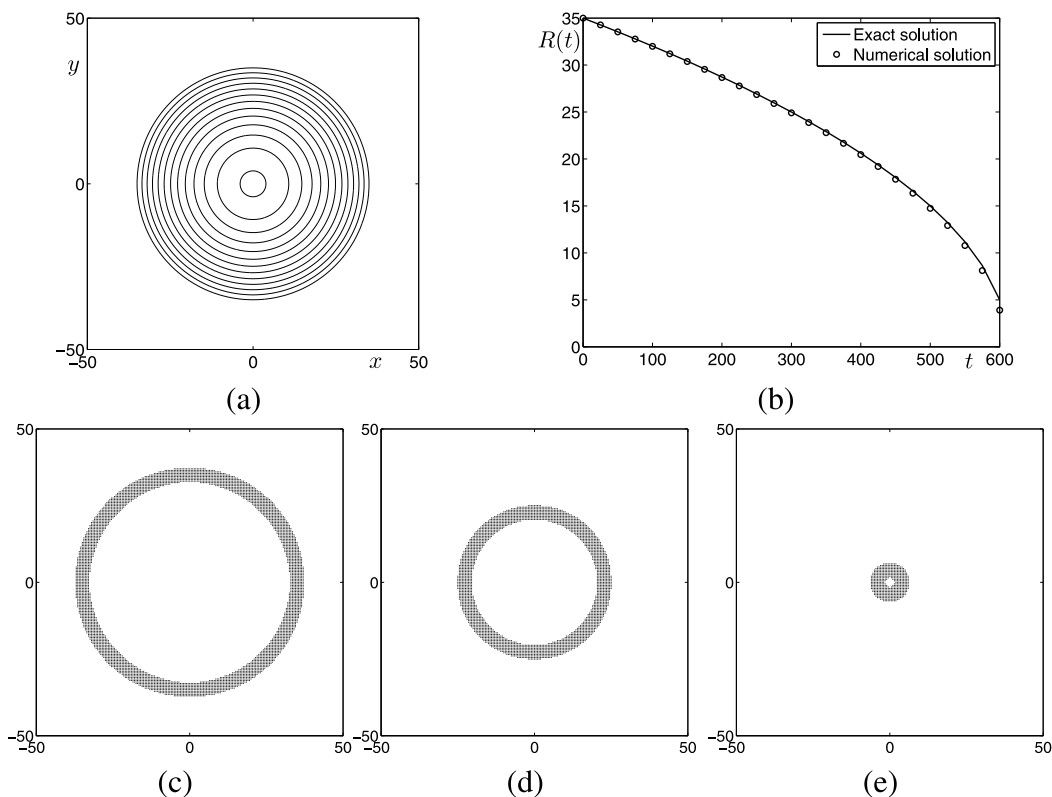$$\phi(x, y, 0) = \tanh\frac{30 + 10\cos(9\theta) - \sqrt{x^2 + y^2}}{\sqrt{2}\epsilon_8},$$

3

Fig. 3. Temporal evolutions of (a) zero-level contour of ϕ and (b) radius $R(t)$. Discrete narrow band domains $\tilde{\Omega}_h^n$ used at (c) $t = 0$, (d) $t = 350$, and (e) $t = 600$.

where θ is the angle made by the vector (x, y) and the x-axis. Fig. 4(a) and (b) show the temporal evolutions of the interface from $t = 0$ to $t = 50$ and from $t = 60$ to $t = 470$, respectively. We use the numerical parameters as $\epsilon = \epsilon_8$, $h = 0.25$, and $\Delta t = 0.2h^2$. Depending on the sign of the curvature of the interface, the tips and the gaps of the star move inward and outward. Once it becomes circular shape, the interface shrinks and then eventually disappears. Fig. 4(c) and (d) show the narrow band domains $\tilde{\Omega}_h^n$ with interfaces at $t = 10$ and $t = 470$, respectively.

3.3. Change of area enclosed by a closed-curve

According to the mathematical theory [22], the area enclosed by a closed-curve decreases at the constant rate, -2π. In this test, we investigate the change of area by a maze and circle. Also, for comparison, we assume that the area of the maze and circle is same. Here, we use the initial radius $r = 38.7833$ of the circle, of which area is equal to the area of the maze as shown in Fig. 5(a) at $t = 0$.

Fig. 5(a) and (c) show the temporal evolutions of the curves of the maze and circle, respectively. Here, we used ϵ_4, $h = 0.25$, $\Delta t = 0.2h^2$ on the computational domain $\Omega = (-50, 50) \times (-50, 50)$. Fig. 5(b) and (d) represent the temporal evolutions of the narrow band domains corresponding to (a) and (b), respectively.

In Fig. 6(a), we can observe the temporal evolutions of the enclosed areas of the maze and the circle. As shown in Fig. 6(a), it can be seen that both the areas are almost identical under the motion by mean curvature. In Fig. 6(b) and (c), we plot together curves of the maze and the circle at $t = 0$ and $t = 570\Delta t$, respectively.

3.4. Avoidance principle

Next, we consider avoidance principle [23]: If any two smooth solutions of the mean curvature flow which are disjoint, then they stay disjoint.

By examining the avoidance principle, we proceed with the two disjoint curves. Here, we use $h = 0.3906$, $\Delta t = 0.2h^2$, $\epsilon = \epsilon_4$ on the computational domain $\Omega = (-50, 50) \times (-50, 50)$. Fig. 7(a) shows the temporal evolutions for two originally disjoint curves at $t = 200\Delta t$, $4000\Delta t$, $10000\Delta t$, $11100\Delta t$. Here, the solid and dashed lines are used to identify those two disjoint curves. Fig. 7(b) represents its corresponding time-dependent narrow band domain of Fig. 7(a). We can see that the numerical results show a good agreement with the avoidance principle [23].
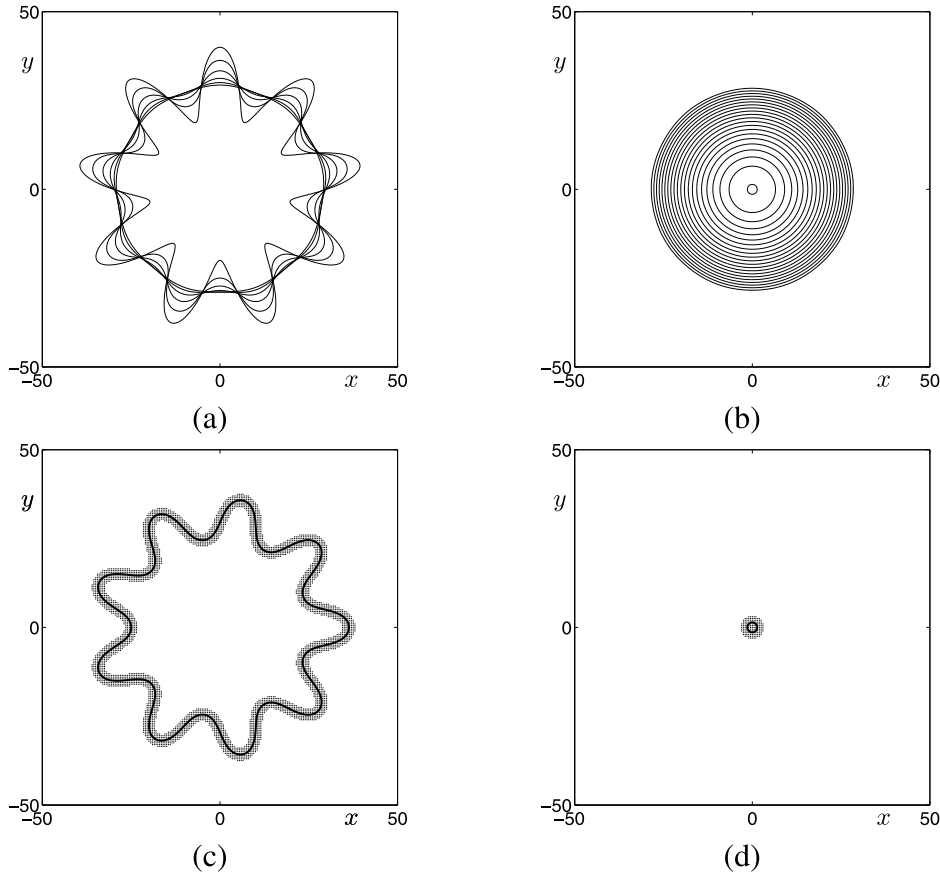
Fig. 4. Temporal evolution of the interface (a) from $t = 0$ to $t = 50$ and (b) from $t = 60$ to $t = 470$. Narrow band domains with interfaces at (c) $t = 10$ and (d) at $t = 470$.

3.5. Huisken's principle [24]

The following one is by Huisken [24]: If the two convex curves γ_1 and γ_2 evolve according to the curvature flow in the plane, and γ_1 contains the closed curve γ_2, then the curve is enclosed by γ_1 for all $t \in [0, \omega)$ for some $\omega > 0$.

The numerical parameters are the same with those above. Fig. 8(a) shows the temporal evolution of two curves at $t = 150\Delta t$, $3000\Delta t$, $7500\Delta t$, $15000\Delta t$. Fig. 8(b) presents the corresponding results on narrow band domain. The solid line indicates the outer curve γ_1 and dashed line indicates the inner curve γ_2. We can find that γ_2 always evolves inside γ_1 as time proceeds.

3.6. Grayson's convexity theorem

In this section, we confirm the Grayson's convexity theorem [25], that a non-convex embedded curve converges to a round circle, using a numerical test. We start the numerical simulation with a start-shaped initial condition and the other parameters are used as the same value in the previous case. Fig. 9(a) shows the temporal evolution of the curve (solid line) with curvature (arrow) at $t = 90\Delta t$, $900\Delta t$, $2700\Delta t$, $9000\Delta t$. Here, the discrete curvature at $\mathbf{X}_l^n$ along the contour is defined as

$$\frac{1}{\Delta s_{l+1/2}} \left(\frac{\mathbf{X}_{l+1}^n - \mathbf{X}_l^n}{\Delta s_{l+1}} - \frac{\mathbf{X}_l^n - \mathbf{X}_{l-1}^n}{\Delta s_l} \right), \tag{3}$$

where $l = 1, \ldots, M$ is the index of a discrete point, $\mathbf{X}_l^n = (X_l^n, Y_l^n)$, on the contour and we set $\mathbf{X}_0^n = \mathbf{X}_M^n$ and $\mathbf{X}_{M+1}^n = \mathbf{X}_1^n$. Also, we use the notion $\Delta s_l = \sqrt{(X_l - X_{l-1})^2 + (Y_l - Y_{l-1})^2}$ and $\Delta s_{l+1/2} = (\Delta s_l + \Delta s_{l+1})/2$. As shown in Fig. 9(a), the curvature along the contour contains the positive and negative values at $t = 90\Delta t$, and then the values of curvature become negative at later times. Fig. 9(b) are the corresponding narrow band domains.
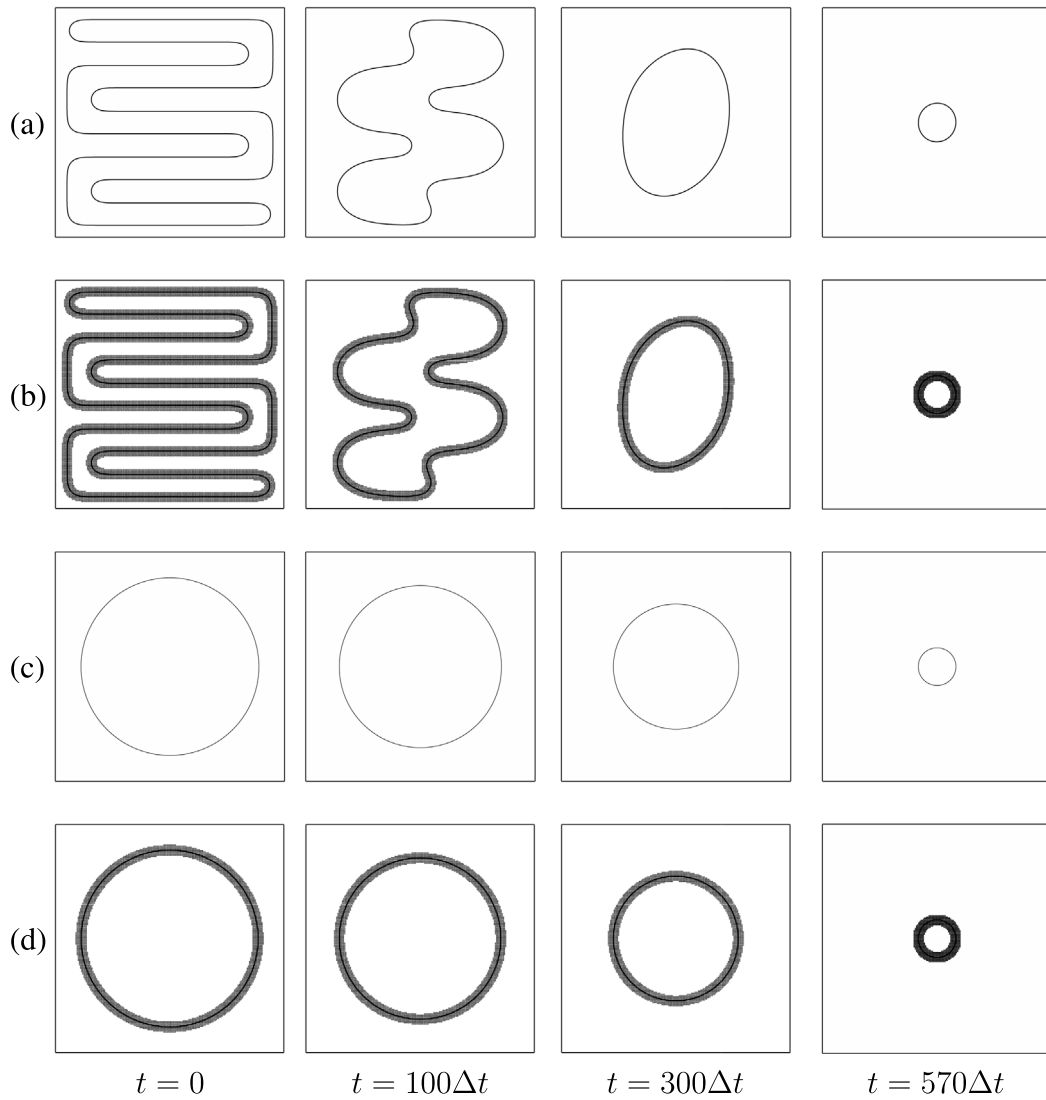
Fig. 5. Temporal evolutions of the curves of (a) maze and (c) circle at $t = 0$, $100\Delta t$, $300\Delta t$, and $570\Delta t$. Narrow band domains of (b) maze and (d) circle used at the corresponding time.
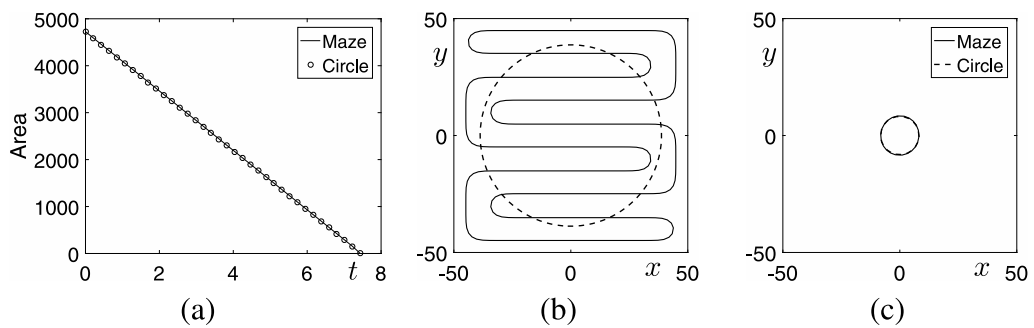

Fig. 6. (a) Temporal evolution of the enclosed areas of the maze and the circle. Plots of the curves of the maze and the circle at (b) $t = 0$ and (c) $t = 570\Delta t$.
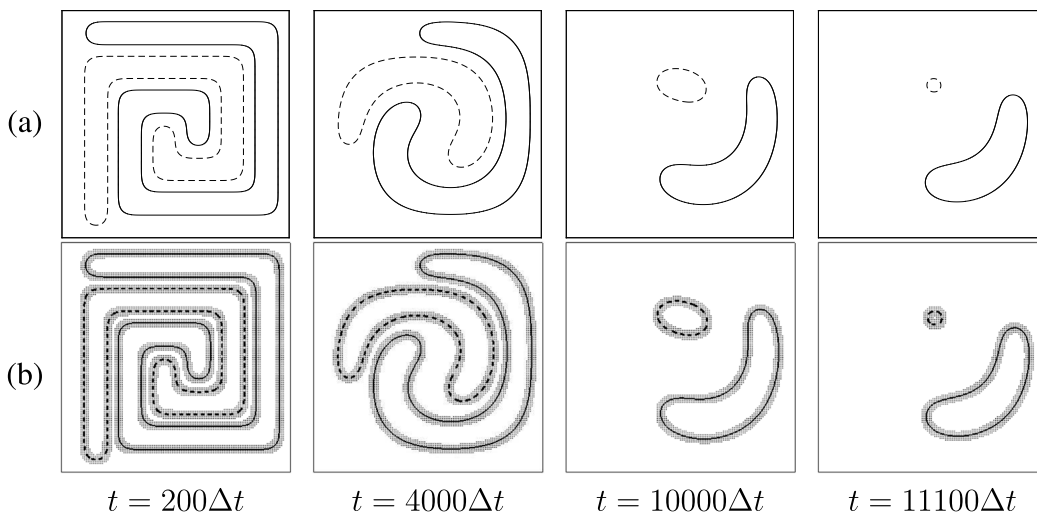
Fig. 7. (a) Temporal evolutions of two disjoint curves. (b) Two curves on its corresponding narrow band domain.
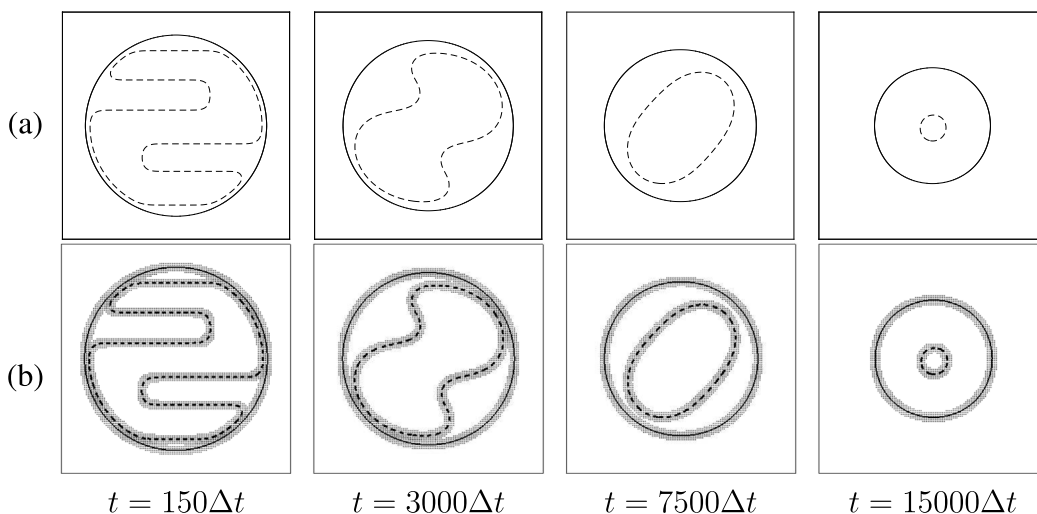

Fig. 8. (a) Temporal evolutions of γ_1 and γ_2. (b) Two curves on its corresponding narrow band domain.

Now, in order to confirm the formation of circle as time proceeds, we compute the temporal evolution of $L^2/(A\pi)$, where L and A denote the total length and area of the curve, respectively. Here, the discrete forms of L and A are defined as

$$L(\mathbf{X}) = \sum_{l=1}^{M} \Delta s_l, \quad A(\mathbf{X}) = \frac{1}{2} \left| \sum_{l}^{M} (X_l Y_{l+1} - Y_l X_{l+1}) \right|.$$

In the case of a circle, we have $L^2/(A\pi) = 4$.

Fig. 10 shows the temporal evolution of $L^2/(A\pi)$ and we can find that the numerical result (thin solid line with circle markers) converges to 4 (thick solid line) as time proceeds. The embedded figures indicate the curvature distribution along the interface at the corresponding times.

3.7. Comparison with multigrid method

To demonstrate the efficiency of the proposed method, we compare the CPU times calculated by the proposed adaptive method and the multigrid method [26]. The initial condition is chosen as $\phi(x, y, 0) = \tanh\left[(30 - \sqrt{x^2 + y^2})/(\sqrt{2}\epsilon)\right]$ on $(-50, 50) \times (-50, 50)$ and $\epsilon = \epsilon_{20}$ is taken. We use $h = 100/256$, $\Delta t = 0.2h^2$ for the proposed method and $\Delta t = 0.2h^2$, $0.8h^2$, $3.2h^2$, $12.8h^2$ for the multigrid method with a tolerance 10^{-8}.
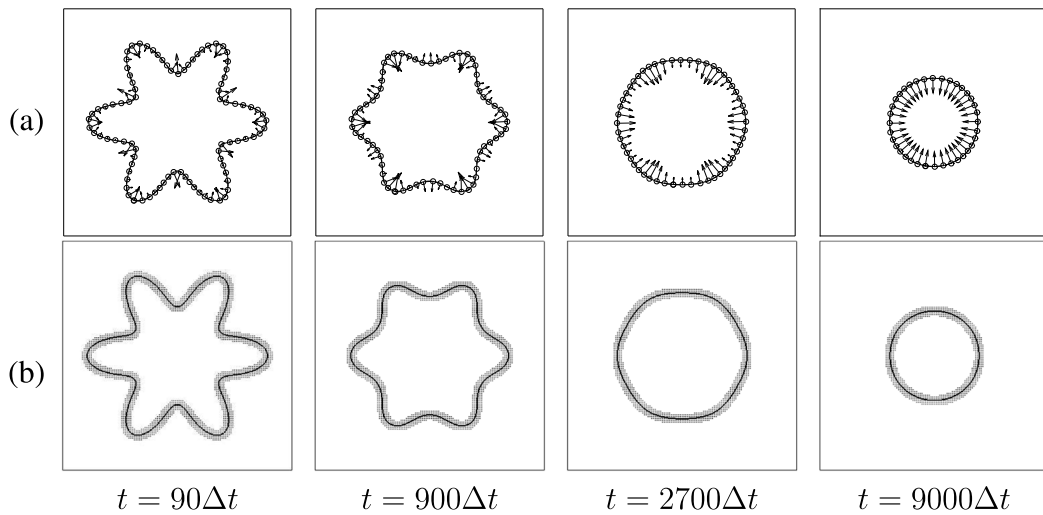
Fig. 9. (a) Temporal evolution of star-shaped curve and (b) its corresponding time-dependent narrow band domain.
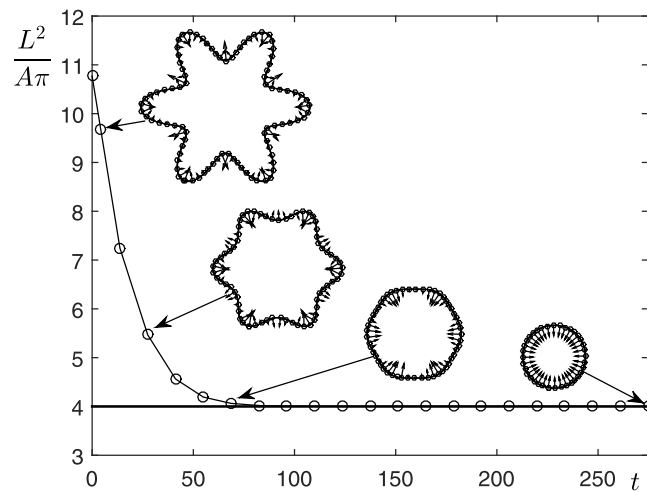

Fig. 10. Temporal evolution of $L^2/(A\pi)$. The embedded figures indicate the curvature distribution along the interface at the corresponding times.
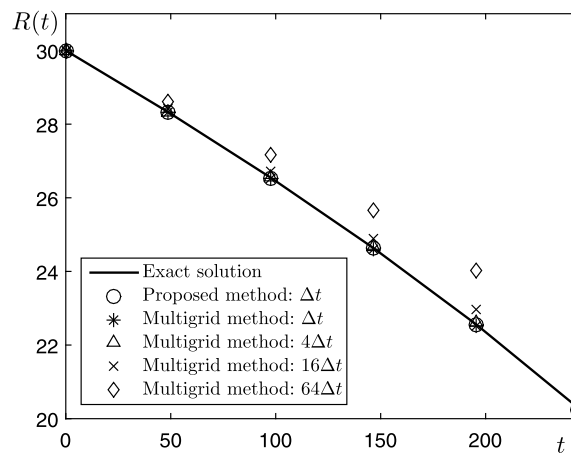

Fig. 11. Evolution of radius for proposed method and multigrid method.

Table 1
Ratios of CPU times between the proposed method and the multigrid method. Here, different case means the time step used in the multigrid method.

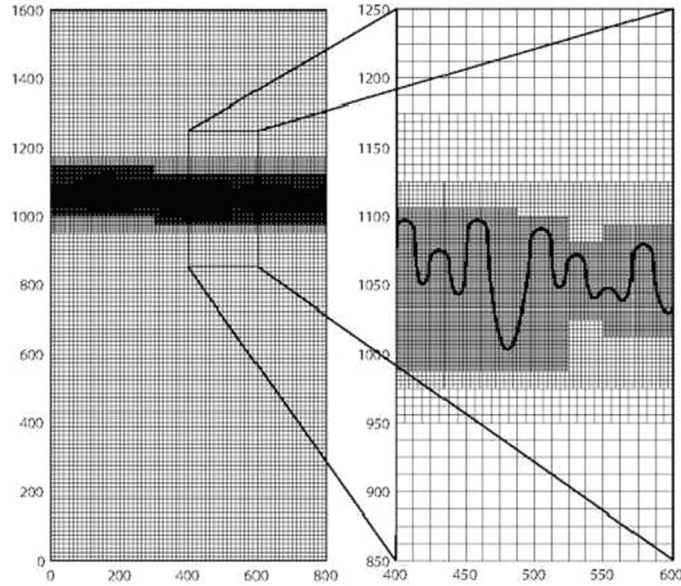| Case	Δt	$4\Delta t$	$16\Delta t$	$64\Delta t$
Ratio	23.1274	8.3240	2.8528	0.6743

Fig. 12. (Left) There are four levels, and the effective fine grid resolution is 1024×2048. This figure displays the fingering phenomenon at $t = 7800$. (Right) A close-up view of the mesh refinement around the front.
Source: Reprinted from Antepara et al. [27] with permission from Springer.

Fig. 11 shows the comparison results between the proposed method and the multigrid method up to time $t = 244.14$. We can find that the numerical result of evolution of radius for the proposed method agrees well with exact solution. The numerical results with small time steps for the multigrid method show a good agreement with exact solution. However, the results with large time steps show inaccurate results.

Table 1 shows the ratios of CPU time for the computation up to time $t = 244.14$. The ratio is defined as the quotient between the CPU times for the multigrid method and the proposed method. As we can see, the multigrid method obviously uses more CPU time than the proposed method and a larger time step for the multigrid method results in a smaller ratio with a less accurate result.

4. Discussion

In this paper, we focused on the practical numerical method to solve the AC equation. This method has merits in simple approach and fast calculation on the refined grid. In this section, we discuss possible applications of the proposed method for the AC equation. As previously mentioned, the AC equation has been applied to many problems and applications such as image inpainting [2], mean curvature flows [3,4], phase transitions [5], multimaterial topology optimization [6], image segmentation [7], and crystal growth [8]. Among them, we introduce a couple of examples.

• **Thin film** : In order to simulate the thin capillary driven films, the following fourth-order nonlinear equation can be used

$$h_t + (h^2 - h^3)_y = -\epsilon^3 \nabla \cdot (h^3 \nabla \Delta h). \tag{4}$$

Here, $h(x, y, t)$ is the variable for thickness of thin liquid layer on an inclined surface, which is driven by thermally created surface tension gradients and influenced by gravity. By splitting Eq. (4) into a system, we obtain

$$h_t + f_y(h) = \nabla \cdot (M(h)\nabla \mu), \tag{5}$$
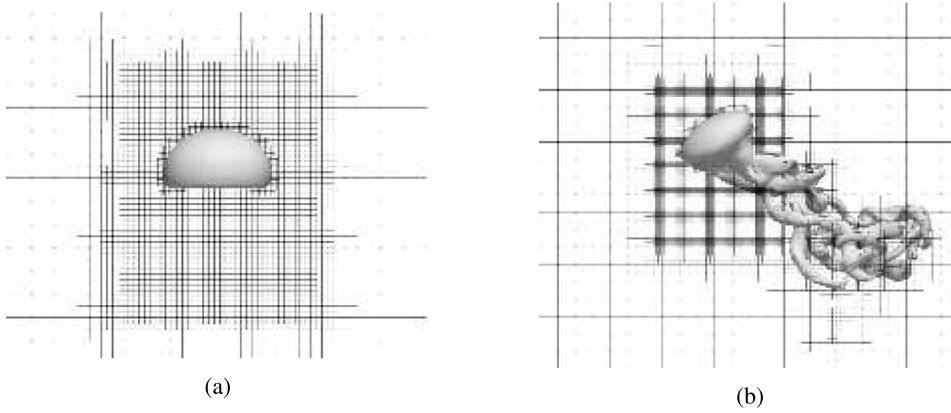
$$\mu = -\epsilon^3 \Delta h, \tag{6}$$

9

(a)   (b)

Fig. 13. Numerical results of the wobbling bubble test on the adaptive grid.
Source: Reprinted from Antepara et al. [31] with permission from Elsevier.

where $f(h) = h^2 - h^3$ and $M(h) = h^3$. In Ref. [27,28], Eqs. (5) and (6) are solved by an adaptive finite difference method with rectangular grid patches dynamically following the front motion.

Fig. 12 shows the main numerical results in Ref. [27]. In Fig. 12, the enlarged view (right) illustrates the four grid levels around the front which is used by the adaptive mesh refinement.

- **Multiphase fluid** : Two immiscible incompressible fluids with surface tension force are described by the Navier–Stokes equation [29] as

$$\frac{\partial(\rho\mathbf{u})}{\partial t} + \mathbf{u} \cdot \nabla\mathbf{u} = -\nabla p + \frac{1}{Re}\Delta\mathbf{u} + \mathbf{F}_s(\phi),$$
$$\nabla \cdot \mathbf{u} = 0,$$

where $\mathbf{u}$ is the fluid velocity, p is the pressure, Re is the Reynolds number, and $\mathbf{F}_s$ is the surface tension of the interface. The interfacial force $\mathbf{F}_s(\phi)$ is given as

$$\mathbf{F}_s = -\frac{3\sqrt{2}\epsilon}{4We}\nabla \cdot \left(\frac{\nabla\phi}{|\nabla\phi|}\right)|\nabla\phi|\nabla\phi,$$

where We is the Weber number [30]. The governing equation of the order parameter ϕ is given by the following phase-field equation:

$$\frac{\partial\phi}{\partial t} + \nabla \cdot (\phi\mathbf{u}) = \frac{1}{Pe}\left(-F'(\phi) + \epsilon^2\Delta\phi\right) + \beta(t)\sqrt{F(\phi)},$$

where Pe is the Peclet number, $F(\phi) = 0.25(\phi^2 - 1)^2$, ϵ is a positive constant, and $\beta(t)$ is a non-constant Lagrange multiplier for the mass conservation. This equation can be used to simulate the wobbling bubble. As an example, Fig. 13 shows the results of wobbling bubble test on the adaptive refinement mesh around the bubble. See Ref. [31] for more detailed explanation of the numerical test.

- **Tumor growth** : First, we denote ϕ_V, ϕ_D, and ϕ_H by the volume fraction of viable tumor, dead tumor, and healthy tissue, respectively [32,33], which satisfy $\phi_H + \phi_V + \phi_D = 1$. With the total tumor volume fraction $\phi_T = \phi_V + \phi_D$, we simplify the mathematical model as follows.

$$\frac{\partial\phi_T}{\partial t} = M\nabla(\phi_T\nabla\mu) + S_T - \nabla \cdot (\mathbf{u}_S\phi_T),$$
$$\mu = f'(\phi_T) - \epsilon^2\nabla^2\phi_T,$$

where $M > 0$ is the mobility constant related to phase separation between ϕ_T and ϕ_H. S_T is the net source of ϕ_T. See Ref. [33] for further explanation of the other parameters. Furthermore, the dynamical equation for ϕ_D is used as

$$\frac{\partial\phi_D}{\partial t} = M\nabla \cdot (\phi_D\nabla\mu) + S_D - \nabla \cdot (\mathbf{u}_S\phi_D),$$

where S_D is the net source of ϕ_D. Therefore, the viable tumor tissue volume fraction is evaluated by $\phi_V = \phi_T - \phi_D$. Fig. 14 shows the temporal evolution of the contours $\phi_V = 0.5$ on the adaptive mesh with three levels of refinement.
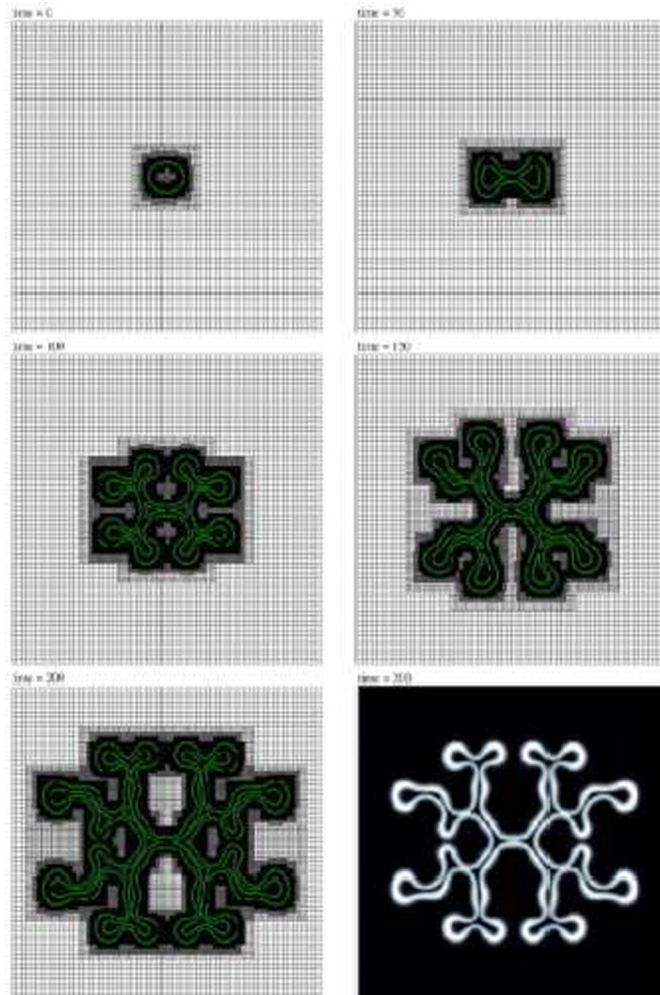
Fig. 14. Evolution of the contours $\phi_T = 0.5$ with the adaptive grid.
Source: Reprinted from Wise et al. [33] with permission from Elsevier.

Here, the bottom right figure shows the full viable cell region which the white and black color corresponds to $\phi_V \approx 1$ and $\phi_V \approx 0$. As shown in Fig. 14, the viable cells are located between the inner and outer contours. Furthermore, the contour of $\phi_V = 0.5$ is increasing as the time goes on.

The above examples are obtained with conventional adaptive mesh techniques. However, it is not easy to implement because the program code is very heavy and complex. Therefor, our proposed method can be useful in implementing the adaptive code.

5. Conclusions

In this paper, we presented a simple and practical explicit adaptive FDM for the AC equation in two-dimensional space. We used a time-dependent adaptive narrow band domain embedded in the uniform discrete rectangular domain. We demonstrated the high performance of the proposed adaptive method for the AC equation through various computational experiments. The numerical results were consistent with theoretical results. In particular, the comparison result with a multigrid method for an implicit scheme showed the superior performance of the proposed method in CPU time over the multigrid method under the condition of equivalent accuracy. As a future research work, we plan to simulate two-phase fluid flow [34] using the proposed explicit adaptive algorithm.

Declaration of competing interest

The authors declare that they have no known competing financial interests or personal relationships that could have appeared to influence the work reported in this paper.

Acknowledgments

References

[1] S.M. Allen, J.W. Cahn, A microscopic theory for antiphase boundary motion and its application to antiphase domain coarsening, Acta Mater. 27 (6) (1979) 1085–1095.
[2] J.A. Dobrosotskaya, A.L. Bertozzi, A wavelet-Laplace variational technique for image deconvolution and inpainting, IEEE Trans. Image Process. 17 (5) (2008) 657–663.
[3] X. Feng, A. Prohl, Numerical analysis of the Allen-Cahn equation and approximation for mean curvature flows, Numer. Math. 94 (1) (2003) 33–65.
[4] D. Jeong, Y. Li, Y. Choi, M. Yoo, D. Kang, J. Park, J. Choi, J. Kim, Numerical simulation of the zebra pattern formation on a three-dimensional model, Physica A 475 (2017) 106–116.
[5] M. Gokieli, L. Marcinkowski, Modelling phase transitions in alloys, Nonlinear Anal. Theory Methods Appl. 63 (5-7) (2005) e1143–e1153.
[6] R. Tavakoli, Multimaterial topology optimization by volume constrained Allen-Cahn system and regularized projected steepest descent method, Comput. Methods Appl. Mech. Engrg. 276 (2014) 534–565.
[7] M. Benes, V. Chalupecky, K. Mikula, Geometrical image segmentation by the Allen-Cahn equation, Appl. Numer. Math. 51 (2–3) (2004) 187–205.
[8] A.A. Wheeler, W.J. Boettinger, G.B. McFadden, Phase-field model for isothermal phase transitions in binary alloys, Phys. Rev. A 45 (10) (1992) 7424–7433.
[9] T. Hou, K. Wang, Y. Xiong, X. Xiao, S. Zhang, Discrete maximum-norm stability of a linearized second-order finite difference scheme for Allen-Cahn equation, Numer. Anal. Appl. 10 (2) (2017) 177–183.
[10] S. Zhai, X. Feng, Y. He, Numerical simulation of the three dimensional Allen-Cahn equation by the high-order compact ADI method, Comput. Phys. Comm. 185 (10) (2014) 2449–2455.
[11] J. Niu, M. Xu, G. Yao, An efficient reproducing kernel method for solving the Allen-Cahn equation, Appl. Math. Lett. 89 (2019) 78–84.
[12] H.G. Lee, J.Y. Lee, A semi-analytical Fourier spectral method for the Allen-Cahn equation, Comput. Math. Appl. 68 (3) (2014) 174–184.
[13] H. Liu, A. Cheng, H. Wang, J. Zhao, Time-fractional Allen-Cahn and Cahn-Hilliard phase-field models and their numerical investigation, Comput. Math. Appl. 76 (8) (2018) 1876–1892.
[14] M. Inc, A. Yusuf, A.I. Aliyu, D. Baleanu, Time-fractional Cahn-Allen and time-fractional Klein-Gordon equations: Lie symmetry analysis, explicit solutions and convergence analysis, Physica A 493 (2018) 94–106.
[15] F. Guillen-Gonzalez, G. Tierra, Second order schemes and time-step adaptivity for Allen-Cahn and Cahn-Hilliard models, Comput. Math. Appl. 68 (8) (2014) 821–846.
[16] A. Shah, M. Sabir, M. Qasim, P. Bastian, Efficient numerical scheme for solving the Allen-Cahn equation, Numer. Methods Partial Differential Equations 34 (5) (2018) 1820–1833.
[17] X. Xiao, D. Gui, X. Feng, A highly efficient operator-splitting finite element method for 2D/3D nonlinear Allen-Cahn equation, Internat. J. Numer. Methods Heat Fluid Flow 27 (2) (2017) 530–542.
[18] C. Li, Y. Huang, N. Yi, An unconditionally energy stable second order finite element method for solving the Allen-Cahn equation, J. Comput. Appl. Math. 353 (2018) 38–48.
[19] D. Jeong, J. Kim, Fast and accurate adaptive finite difference method for dendritic growth, Comput. Phys. Comm. 236 (2019) 95–103.
[20] D. Jeong, J. Kim, An explicit hybrid finite difference scheme for the Allen-Cahn equation, J. Comput. Appl. Math. 340 (2018) 247–255.
[21] M. Inc, A. Yusuf, A.I. Aliyu, D. Baleanu, Time-fractional Cahn-Allen and time-fractional Klein-Gordon equations: Lie symmetry analysis, explicit solutions and convergence analysis, Physica A 493 (2018) 94–106.
[22] M. Gage, R.S. Hamilton, The heat equation shrinking convex plane curves, J. Differential Geom. 23 (1) (1986) 69–96.
[23] X.P. Zhu, Lectures on Mean Curvature Flows, 32, AMS, International Press, Somerville, 2002.
[24] G. Huisken, Flow by Mean Curvature of Convex Surfaces into Spheres, Australian National University, Centre for Mathematical Analysis, 1984.
[25] M.A. Grayson, The heat equation shrinks embedded plane curves to round points, J. Differential Geom. 26 (2) (1987) 285–314.
[26] Y. Li, H.G. Lee, D. Jeong, J.S. Kim, An unconditionally stable hybrid numerical method for solving the Allen-Cahn equation, Comput. Math. Appl. 60 (6) (2010) 1591–1606.
[27] J. Kim, Adaptive mesh refinement for thin-film equations, J. Korean Phys. Soc. 49 (5) (2006) 1903.
[28] Y. Li, D. Jeong, J. Kim, Adaptive mesh refinement for simulation of thin film flows, Meccanica 49 (1) (2014) 239–252.
[29] D. Jeong, J. Kim, Conservative Allen-Cahn-Navier-Stokes system for incompressible two-phase fluid flows, Comput. Fluids 156 (2017) 239–246.
[30] J. Kim, A continuous surface tension force formulation for diffuse-interface models, J. Comput. Phys. 204 (2) (2005) 784–804.
[31] O. Antepara, N. Balcazar, J. Rigola, A. Oliva, Numerical study of rising bubbles with path instability using conservative level-set and adaptive mesh refinement, Comput. Fluids 187 (2019) 83–97.
[32] S.M. Wise, J.S. Lowengrub, H.B. Frieboes, V. Cristini, Three-dimensional multispecies nonlinear tumor growth?I: model and numerical method, J. Theoret. Biol. 253 (3) (2008) 524–543.
[33] S.M. Wise, J.S. Lowengrub, V. Cristini, An adaptive multigrid algorithm for simulating solid tumor growth using mixture models, Math. Comput. Model. 53 (1–2) (2011) 1–20.
[34] A. Toghaniyan, M. Zarringhalam, O.A. Akbari, G.A.S. Shabani, D. Toghraie, Application of lattice Boltzmann method and spinodal decomposition phenomenon for simulating two-phase thermal flows, Physica A 509 (2018) 673–689.